AGU PUBLICATIONS

JGR

Journal of Geophysical Research: Space Physics

RESEARCH ARTICLE

10.1002/2016JA023788

Special Section:
Magnetospheric Multiscale (MMS) mission results throughout the first primary mission phase

Key Points:
- Mapping data to a parametric space captures many of the typical EDR signatures
- The EDR is offset northward and earthward relative to the topological X line
- EDR extent is 2–3 km in the normal direction, >20 km in the tangential direction

Correspondence to:
L. Alm,
love@spam.sr.unh.edu

Citation:
Alm, L., et al. (2017), EDR signatures observed by MMS in the 16 October event presented in a 2-D parametric space, *J. Geophys. Res. Space Physics*, *122*, 3262–3276, doi:10.1002/2016JA023788.

Received 8 DEC 2016
Accepted 27 JAN 2017
Accepted article online 1 FEB 2017
Published online 22 MAR 2017

EDR signatures observed by MMS in the 16 October event presented in a 2-D parametric space

L. Alm[1], M. R. Argall[1], R. B. Torbert[1,2], C. J. Farrugia[1], J. L. Burch[2], R. E. Ergun[3], C. T. Russell[4], R. J. Strangeway[4], Y. V. Khotyaintsev[5], P.-A. Lindqvist[6], G. T. Marklund[6], B. L. Giles[7], and J. Shuster[7,8]

[1]Space Science Center, University of New Hampshire, Durham, New Hampshire, USA, [2]Southwest Research Institute, San Antonio, Texas, USA, [3]Laboratory for Atmospheric and Space Physics, University of Colorado Boulder, Boulder, Colorado, USA, [4]IGPP/EPSS, University of California, Los Angeles, California, USA, [5](IRF) Swedish Institute of Space Physics, Uppsala, Sweden, [6]KTH Royal Institute of Technology, Stockholm, Sweden, [7]NASA Goddard Space Flight Center, Greenbelt, Maryland, USA, [8]College of Computer, Mathematical, and Natural Sciences, University of Maryland, College Park, Maryland, USA

Abstract We present a method for mapping the position of satellites relative to the X line using the measured B_L and B_N components of the magnetic field and apply it to the Magnetospheric multiscale (MMS) encounter with the electron diffusion region (EDR) which occurred on 13:07 UT on 16 October 2015. Mapping the data to our parametric space succeeds in capturing many of the signatures associated with magnetic reconnection and the electron diffusion region. This offers a method for determining where in the reconnection region the satellites were located. In addition, parametric mapping can also be used to present data from numerical simulations. This facilitates comparing data from simulations with data from in situ observations as one can avoid the complicated process using boundary motion analysis to determine the geometry of the reconnection region. In parametric space we can identify the EDR based on the collocation of several reconnection signatures, such as electron nongyrotropy, electron demagnetization, parallel electric fields, and energy dissipation. The EDR extends 2–3 km in the normal direction and in excess of 20 km in the tangential direction. It is clear that the EDR occurs on the magnetospheric side of the topological X line, which is expected in asymmetric reconnection. Furthermore, we can observe a north-south asymmetry, where the EDR occurs north of the peak in out-of-plane current, which may be due to the small but finite guide field.

1. Introduction

Magnetic reconnection is a process which occurs in many places throughout our universe. At the Sun, magnetic reconnection drives energetic events such as flares and coronal mass ejections. In the magnetosphere, magnetic reconnection provides energy for geomagnetic storms and aurora, making it an influential factor in modifying the near-Earth environment. While magnetic reconnection is rather well understood on the larger scales, we have yet to understand the electron scale physics which lies at the heart of magnetic reconnection and the mechanisms responsible for breaking and merging of magnetic field lines.

In the electron diffusion region (EDR) there are changes in the magnetic topology, breaking of the frozen-in condition of ideal MHD, and magnetic energy is converted into particle energy. Therefore, measurements of these properties are key to identifying magnetic reconnection and the EDR.

At the X line, magnetic field lines break and merge, changing the magnetic field from being purely tangential to the magnetopause to having a component along the magnetopause normal. Therefore, observing a finite normal magnetic field is in itself a strong indication of being located close to the X line.

The out-of-plane reconnection electric field, which convects the magnetic field lines toward the X line, is typically on the order of 1 mV/m [*Vaivads et al.*, 2006]. It is thought to be supported by electron pressure nongyrotropy, electron inertial effects, or a combination of the two. Recent particle-in-cell (PIC) simulations of asymmetric reconnection have indicated that the reconnection electric field may be generated by electron inertial effects near the X line and generated by pressure nongyrotropies near the flow stagnation point [*Hesse et al.*, 2005, 2014].

One method for quantifying the pressure nongyrotropy is by calculating the agyrotropy scalar. The agyrotropy scalar is a dimensionless quantity representing the pressure tensor's deviation from a cylindrical symmetry around the local magnetic field. The pressure agyrotropy scalar, $A\Phi_e$ is defined as

$$A\Phi_e = 2\frac{|P_{\perp e1} - P_{\perp e2}|}{P_{\perp e1} + P_{\perp e2}}, \tag{1}$$

where $P_{\perp e1}$ and $P_{\perp e2}$ are the two eigenvalues of the pressure tensor which corresponds to the two eigenvectors perpendicular to the magnetic field [*Scudder and Daughton*, 2008; *Scudder et al.*, 2012]. From its definition it follows that if the pressure is completely gyrotropic $A\Phi_e = 0$ and if the pressure is completely agyrotropic $A\Phi_e = 2$. Alternatively, the full pressure tensor, $\mathbf{P}$, can be decomposed into a gyrotropic component $\mathbf{G}$ and a nongyrotropic component $\mathbf{N}$ so that $\mathbf{P} = \mathbf{G} + \mathbf{N}$. The local degree of nongyrotropy, $D_{\rm ng}$, is a dimensionless quantity defined as

$$D_{\rm ng} = \frac{\sqrt{\sum_{i,j} N_{ij}^2}}{Tr\left(\mathbf{P}\right)}, \tag{2}$$

which is independent of the choice of vector basis for the pressure tensor [*Aunai et al.*, 2013]. Following this definition, a completely gyrotropic pressure tensor corresponds to $D_{\rm ng} = 0$. The main difference between $A\Phi_e$ and $D_{\rm ng}$ is that the former calculates the nongyrotropy in the plane perpendicular to the magnetic field, while the latter is more general as it calculates the measure of nongyrotropy using the full 3×3 pressure tensor.

As particles approach the low B field region surrounding the X line, ion ceases being frozen in and can be considered demagnetized. Further in, closer to the X line, the electrons become demagnetized.

Meaning that $\mathbf{E} + \mathbf{v} \times \mathbf{B} \neq 0$, where $\mathbf{E}$ is the electric field, $\mathbf{v}$ is the velocity of the particle, and $\mathbf{B}$ is the magnetic field. This is supported by in situ observations of reconnection [e.g., *Mozer et al.*, 2002]. The Lorentz ratio, δ_e, is a scalar measure of the degree of demagnetization, which compares the strength of the electric and magnetic forces in the electron rest frame. It is defined as

$$\delta_e = \frac{|\mathbf{E} + \mathbf{v}_e \times \mathbf{B}|}{w_{\perp e} B}, \tag{3}$$

where $\mathbf{v}_e$ is the electron bulk velocity, e is elementary charge, and $w_{\perp e}$ is the thermal speed of the electrons [*Scudder and Daughton*, 2008; *Scudder et al.*, 2008]. A particle can be considered to be fully demagnetized if $\delta_e > 1$ [*Maynard et al.*, 2012].

In the ion diffusion region, the differential motion of the demagnetized ions and the magnetized electrons sets up a Hall current, perpendicular to both the magnetic and electric fields [*Sonnerup*, 1979]. The Hall current results in two characteristic magnetic and electric field signatures. For symmetric reconnection, the Hall magnetic field consists of a quadrupolar signature in the out-of-plane magnetic field [*Nagai et al.*, 2001]. Two-dimensional PIC simulations of asymmetric reconnection have found that the Hall magnetic field tends to be stronger on the magnetosheath side [*Pritchett*, 2008; *Pritchett and Mozer*, 2009a; *Muzamil et al.*, 2014].

The Hall electric field is associated with the inflow region. In symmetric reconnection it manifests as a bipolar electric field, on the order of some tens of mV/m, pointing toward the X line [*Vaivads et al.*, 2004, 2006]. In asymmetric reconnection the Hall electric field is typically stronger on the magnetosphere side of the X line and can sometimes appear as a nearly unipolar signature [*Pritchett*, 2008; *Pritchett and Mozer*, 2009a].

The conversion of magnetic energy into kinetic energy which occurs in the electron diffusion region is a dissipative process, implying that $\mathbf{j} \cdot \mathbf{E} > 0$, where $\mathbf{j}$ is the current density. By utilizing the electric field and current in the electron rest frame, one can calculate the electron rest frame energy dissipation, D_e, which is defined as

$$D_e = \mathbf{j}' \cdot \mathbf{E}' = \gamma \left[\mathbf{j} \cdot \left(\mathbf{E} + \mathbf{v}_e \times \mathbf{B}\right) - \rho_c \mathbf{v}_e \cdot \mathbf{E}\right], \tag{4}$$

where ρ_c is the charge density and γ is the Lorentz factor of the electrons ($[1 - \left(v_e/c\right)^2]^{-1/2}$) [*Zenitani et al.*, 2011a, 2011b]. One advantage of this measurement is that it is Lorentz invariant and thereby insensitive to the motion of the X line relative to the spacecraft. An alternative measurement of the electron energization is to look at the rate of energization. It describes the energy gain per electron cyclotron period, normalized to the initial thermal energy. The rate of electron energization, ϵ_e, can be written as

$$\epsilon_e = \frac{2\pi e \mathbf{E} \cdot \mathbf{v}_e}{\Omega_{ce} k T_e}, \tag{5}$$

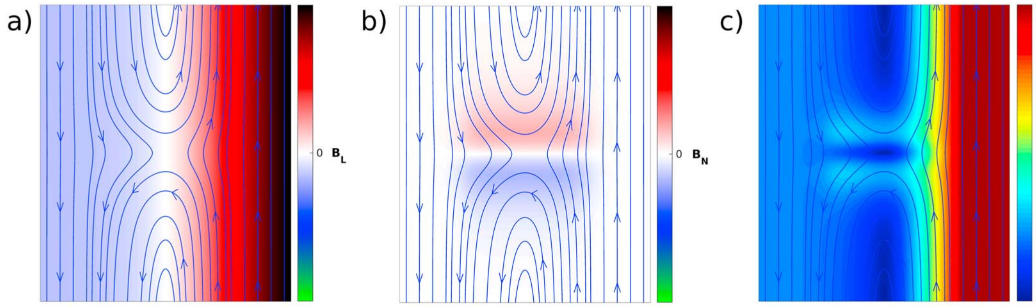

Figure 1. Model of the magnetic topology near the X line (a) tangential magnetic field (B_L), (b) normal magnetic field (B_N), and (c) magnetic field strength ($|B|$).

where Ω_{ce} is the electron cyclotron period, k is Boltzmann's constant, and T_e the electron temperature [*Scudder et al.*, 2012].

In studying magnetic reconnection the position of the spacecraft, relative to the X line, can be inferred from several measurable quantities, such as the magnetic field and plasma bulk velocity. In practice, some of these estimates are of a qualitative nature and are difficult to use for comparing data from different satellites, different reconnection events, or comparing with results from computer simulations. Quantitative estimates of the satellites position can be achieved through motion analysis of the X line. However, many of the methods for motion analysis rely on assuming either constant velocity or constant acceleration of the X line, which in practice is not always the case. This limits the ability to fully resolve the small-scale structure of the EDR.

This paper presents an alternative method for determining the position of the satellite. We attempt to describe the satellites' position, relative to the X line, in a parametric space based on the observed magnetic field. This method links observations to a point in the magnetic topology rather than to a point in space. The method will be benchmarked using the well-known reconnection event observed by the MMS constellation around 13:07 UT on 16 October 2015 [*Burch et al.*, 2016; *Torbert et al.*, 2016b; *Denton et al.*, 2016].

2. Methods

2.1. Parametric Space

In order to understand the basic premise of parametric space mapping, we start by looking at the magnetic topology of dayside reconnection, described in boundary-normal coordinates. We use the naming convention associated with minimum variance of the magnetic field, where B_L and B_M are the tangential magnetic field components in the maximum and intermediate variance directions and B_N is the normal component, along the minimum variance direction [*Paschmann and Daly*, 1998]. It is worth noting that our method is not dependent on the method used to determine the orientation of the magnetopause. There are a number of single and multiple spacecraft methods which can be used to determine the orientation of the magnetopause, though the definition of their respective vector basis will differ and thereby how the parametric space is defined [*Paschmann and Daly*, 2008; *Haaland et al.*, 2004].

As seen in Figure 1a, the reconnecting tangential component, B_L, is negative on the magnetosheath side of the magnetopause and positive on the magnetosphere side of the magnetopause. Near the X line, reconnection causes the magnetic field to have a component normal to the magnetopause, B_N. As can be seen in Figure 1b, B_N points toward the magnetosphere north of the X line and toward the magnetosheath south of the X line.

In order to map our observations to a suitable parametric space, we first establish a model of the magnetic topology near the X line using boundary-normal coordinates.

We model the reconnection region using simple 2-D X line topology corresponding to dayside reconnection, illustrated in Figure 2. As can be seen in Figure 2a, the reconnecting tangential component, B_L, is negative on the magnetosheath side (to the left), exhibits a monotonic gradient across the parametric space, and is positive on the magnetosphere side of the X line. As a consequence of the reconnection process, the magnetic field exhibits a component normal to the magnetopause, B_N. As can be seen in Figure 2b, north of the X line B_N points toward the magnetosphere, while south of the X line B_N points toward the magnetosheath. As a result, B_N exhibits a monotonic gradient across the parametric space. Consequently, the parametric space

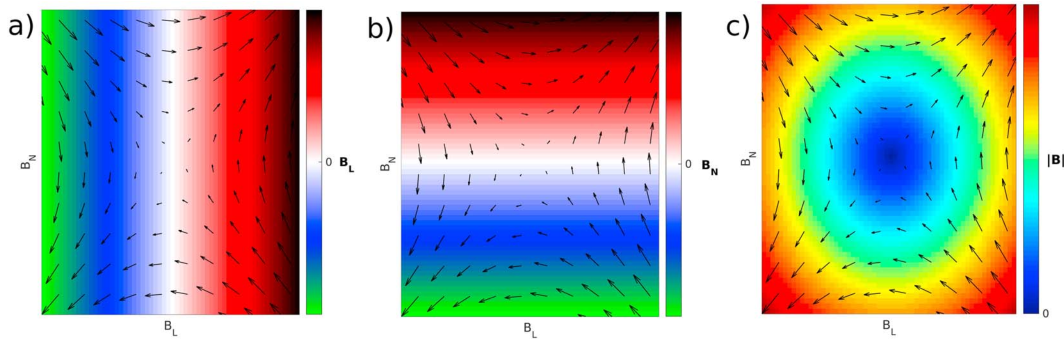

Figure 2. Illustration of the magnetic topology used to define the parametric space. (a) tangential magnetic field (B_L), (b) normal magnetic field (B_N), and (c) magnetic field strength ($|B|$).

has a magnetic null in its center and the total magnitude of B_L and B_N increases monotonically with the distance from the null, Figure 2c. Note that the model does not make any predictions on the spatial scales involved or the gradients in the magnetic field. It is important to make the distinction that in this parametric space one cannot describe magnetic field lines, since they by definition are spatial structures. For this reason, we cannot identify the separatrices in the conventional sense. However, the separatrices are expected to be located near the region where the magnetic field transitions from being predominately tangential to being predominately normal.

In theory, this topology allows for the position of a satellite to be determined unambiguously if B_L and B_N are known. While the B_L gives a robust estimate of the position in the N direction, using B_N to estimate the position in the L direction is more complicated. For the assumed topology $B_N = 0$ is true only near the X line. Since the presence of a finite B_N is a direct consequence of the reconnection process, $B_N = 0$ is also true for magnetopause crossings occurring far from an X line. Therefore, one must exercise caution by only selecting data in close proximity to an X line, where the assumed topology is valid.

Since B_L and B_N are being used to map the satellite's position in the parametric space, they will not exhibit any variations other than those imposed by how the parametric space is defined. As a consequence, only the out-of-plane component, B_M, will exhibit any meaningful variations across the parametric space. The same would be true for any other parameter which could be used to define our parametric grid. For this reason, attempting to increase the accuracy of the mapping to parametric space, by including additional parameters to define it, will as a consequence reduce the amount of data which exhibits meaningful variations across the parametric space.

The data of all MMS satellites were binned and averaged across the parametric space. The choice of bin size depends on two factors. First, the bin must be large enough so that most bins within our region of interest contain data. Additionally, the bin size must be large enough so that a meaningful average can be calculated, avoiding bins containing only single measurements. Second, the bins must be small enough to resolve the structures which are to be studied. The second factor is especially important for the electric field which has a high time resolution and is capable of resolving small-scale, and in some cases bipolar, structures which can be either greatly enhanced or completely suppressed depending on the size of the bin and their position within the bin.

As a compromise, we combine a smaller bin size of 0.5 nT and use a weighted average over the surrounding 5 by 5 set of bins. This allows us to have the statistical advantage of a larger bin, increasing the number of data points, while retaining the advantage of smaller bins in being able to resolve small-scale structures. The data in 5 by 5 set of bins were weighted so that the central bin had a weighting factor of 1; the eight bins immediately surrounding the central bin were given a weighting factor of 1/8 and the outermost 16 bins a weighting factor of 1/16. This puts a greater emphasis on data close to the central bin. In each 5-by-5 set of bins, those bins which contained no data were ignored rather than been treated as having a value of zero. This eliminates the problem of empty bins suppressing the data of adjacent bins. Additionally, the average was only calculated if more than three of the 25 bins contained data. If not, the original value is retained.

Binning and averaging the data assumes that for the quantities we want to study $\langle \partial/\partial t = 0 \rangle$, so that $\mathrm{d}/\mathrm{d}t = \partial/\partial t + \mathbf{v} \cdot \nabla \approx \mathbf{v} \cdot \nabla$. In other words, we assume that the systematic variations observed by the satellites are primarily due to their motion through the reconnection region. The validity of this assumption requires that the analysis is conducted over a short time interval where the average of temporal variations can be assumed to be relatively small.

Binning and averaging the data introduces a degree of error from the inherent uncertainty in estimating the position of the satellite and any purely temporal variations. Vector quantities, which are transformed into boundary-normal coordinates, experience a second order of uncertainty as both their vector value and position in the parametric space are dependent on this coordinate transformation. For this reason one must exercise some caution in interpreting vector data. This is less of a problem for scalar quantities, which are only affected by the uncertainty in their position in the parametric space. This includes the parallel electric fields and parallel currents as they can be calculated from the original data, before converting the vector quantities into boundary-normal coordinates.

2.2. Magnetospheric Multiscale Mission

NASA's Magnetospheric multiscale (MMS) mission was designed for the purpose of studying the electron scale physics of magnetic reconnection. It consists of a constellation of four identical satellites, orbiting the Earth in a highly elliptical equatorial orbit. In order to be able study magnetic reconnection on the electron scale, MMS has been equipped with an instrument suite which offers an unprecedented spatial and temporal resolution, combined with a satellite separation of as little as 10 km [*Burch et al.*, 2016].

The FIELDS instrument suite, which measures electric and magnetic fields, consists of six sensors: three electric field sensors and three magnetic field sensors [*Torbert et al.*, 2016a]. Each MMS satellite is equipped with two sets of double probe sensors, one set making measurements in the spin plane of the satellite and one set along the spin axis of the satellites, allowing for 3-D measurements of the electric field. The Spin-plane Double Probes, which are mounted at the end of 60 m long wire booms, can measure electric fields ranging from DC up to 100 kHz, with a precision of 0.5 mV/m [*Lindqvist et al.*, 2016]. The Axial Double Probes (ADP) are mounted at the end of two 12.67 m long coilable booms, giving it an unprecedented baseline for an instrument of its type. The ADP can measure DC electric fields with a precision of 1 mV/m [*Ergun et al.*, 2016]. The Analog and Digital Fluxgate Magnetometers measure 3-D magnetic fields ranging from DC and up to 64 Hz [*Russell et al.*, 2016]. In addition, the FIELDS suit contains an Electron Drift Instrument that provides an independent measurement of electric fields in the plane perpendicular to the magnetic and a search coil magnetometer measuring magnetic fields ranging from 1 Hz up to 6 kHz [*Torbert et al.*, 2016c; *Le Contel et al.*, 2016].

The Fast Plasma Investigation (FPI) provides 3-D distributions of electrons and ions with energy/charge ratios between 10 eV/q and 30,000 eV/q. Unlike most previous particle spectrometers, FPI does not depend on using the spacecraft spin to achieve full 4π steradian solid angel coverage. Each MMS satellite is equipped with eight FPI spectrometers, four electrons, and four ions, which are able to control their field of view via electrostatic deflection. This gives FPI an unprecedented time resolution, where the full 3-D electron and ion distributions can be measured in 30 ms and 150 ms, respectively [*Pollock et al.*, 2016]. The high time and energy resolution allows us to calculate currents directly from the particle moments instead of using the curlometer method.

The combination of these instruments allows us to measure the key reconnection parameters described in section 1 and determines the position of each satellite in our parametric space.

3. Results

The event we have studied occurred around 13:07:00 UT on 16 October 2015, shortly after the MMS constellation had passed apogee. This event is first the clear observation of the EDR made by MMS and has been the subject of several recent papers [e.g., *Burch et al.*, 2016; *Denton et al.*, 2016; *Torbert et al.*, 2016b]. We will present a brief overview of the event based on the data from MMS 2.

Starting at approximately 13:06:40 UT, MMS observed two magnetopause crossings, one outbound and one inbound. The first (inbound) and second (outbound) crossings of the magnetopause can be identified in Figure 3a from the reversal in B_L. The small-scale structures observed in B_L indicate that the magnetopause exhibits both a large-scale flapping motion over the time scale of tens of seconds and also small-scale, subsecond time scale fluttering. During the second magnetopause crossing, at approximately 13:07:03 UT, MMS 2 observes a null in the reconnecting components of the magnetic field, B_N and B_L.

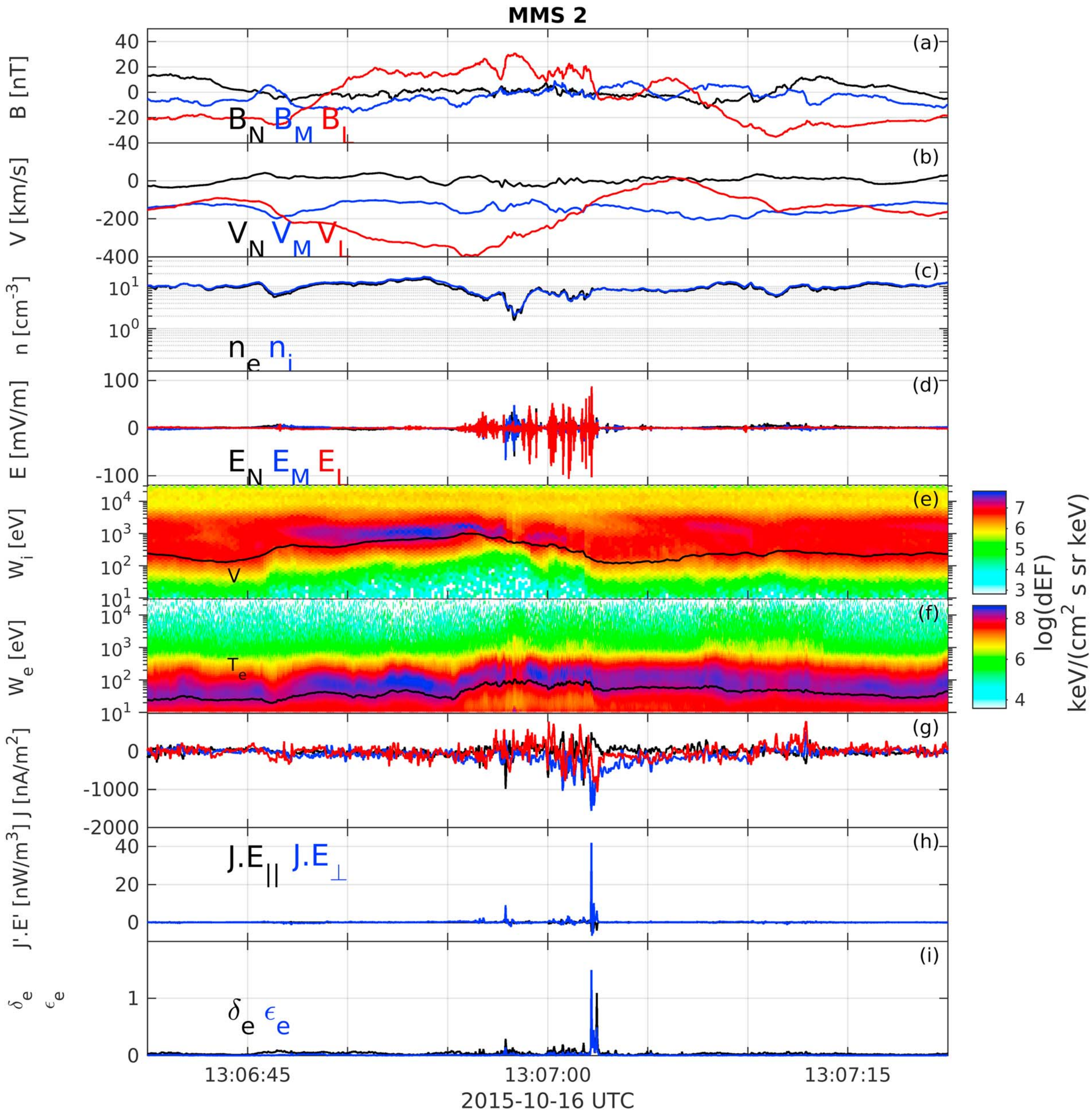

Figure 3. Summary of the event as observed by MMS 2. (a) Magnetic field in boundary-normal coordinates, (b) ion velocity boundary-normal coordinates, (c) number density, (d), electric field boundary-normal coordinates, (e) ion energy spectrogram, (f) electron energy spectrogram, (g) current, (h) electron frame energy dissipation, and (i) Lorentz factor (black) and rate of energization (blue).

As can be seen in Figure 3b, $V_{i,L}$ exhibits a sharp gradient going from approximately −400 km/s to approximately 0 km/s. This is indicative of observing a jet reversal from an X line moving in the $-L$ direction. This indicates that MMS 2 is initially located south of the X line moving northward.

As shown in Figure 3c, there is a clear density asymmetry between the magnetosphere and magnetosheath side. Inside the magnetosphere the electron density is as low as 2 cm^{-3}, whereas the typical value on the magnetosheath side is approximately 10 cm^{-3}.

Between 13:06:55 UT and 13:07:05 UT we can observe strong and rapidly fluctuating electric fields, Figure 3d. These coincide with the region of strong out-of-plane currents seen in Figure 3g, with a peak value of approximately 1500 nA/m^2. The peak out-of-plane current occurs at the same time as Figure 3h exhibits large perpendicular energy dissipation. As can be seen in Figure 3h, both δ_e and ϵ_e exhibit values in excess of 1, indicating that the electrons are demagnetized. This coincides with the observations of crescent-shaped

Table 1. Boundary-Normal Vector Basis in GSE Coordinates[a]

N	M	L
0.7358	−0.5694	0.3665
0.6443	0.7553	−0.1201
−0.2084	0.3245	0.9226

[a]Derived from *Burch et al.* [2016].

electron distribution reported by *Burch et al.* [2016], indicative of particles originating in the magnetosheath meandering across the X line.

As can be concluded from Figure 3, MMS observes a case of asymmetric reconnection, which is to be expected at the magnetopause. Previous papers conclude that the MMS constellation passes through the EDR, which is supported by our observations [*Burch et al.*, 2016; *Denton et al.*, 2016; *Torbert et al.*, 2016b].

In order to study the event in a parametric space, we take the original data from all four MMS satellites during the time period 13:06:49–13:07:07 UT and convert all vector quantities to boundary-normal coordinates. This is performed using the same vector basis used in the previous paper by *Burch et al.* [2016]. The vector basis can be found in Table 1. We convert the original data into a right-hand-orientated *NML* coordinate system, so that N is approximately $+\mathrm{GSE}_X$, M is approximately $+\mathrm{GSE}_Y$, and L is approximately $+\mathrm{GSE}_Z$.

Figure 4 contains the magnetic field data from all four satellites. The X axis is the observed B_L, and the Y axis, which is inverted, is the observed B_N. In the figure, the Sun is located to the left and north is toward the top of the figure. This is equivalent to the geometry used in *Mozer et al.* [2002]. The three lines traced through the parametric space represents the paths of MMS 2–4 during the time period when *Burch et al.* [2016] report observing crescent-shaped electron distributions, where the individual plot markers represent the position of the satellite as it observed the crescent. The distributions of B_N and B_L are not plotted since they were used to define the parametric space.

The large-scale variations of the magnetic field strength, Figure 4a, are largely in agreement with that of our model topology, Figure 2c. The magnetic field strength increases with the distance from the X line. However, there are three clear deviations from this radial symmetry. Near the X line, at $-2 < B_L < 2$ nT, $-1 < B_N < 1$ nT, magnetic field strength exhibits a local maximum, as opposed to the expected minimum. In addition, the magnetic field strength exhibits two linear structures, starting at the X line extending northward and toward the magnetosheath and magnetosphere, respectively. As a result, rather than a radial symmetry, the regions of low magnetic field strength appear as a clover leaf-shaped area.

As a consequence of how the parametric space is defined, the only component of the magnetic field which can account for this enhancement in the magnetic field strength is the out-of-plane component B_M. This can be seen in Figure 4b, where the out-of-plane magnetic field is enhanced in the same regions which exhibits enhanced magnetic field strength. Throughout our parametric space, the average B_M is 3.3 nT, which we interpret as a guide field of the same strength. This is approximately 50% higher than reported in previous papers on this event [*Burch et al.*, 2016; *Denton et al.*, 2016]. Figure 4c illustrates the perturbed out-of-plane magnetic field, $\mathrm{d}B_M$, calculated by subtracting $\langle B_M \rangle$ from the observed B_M. This operation does not change the overall

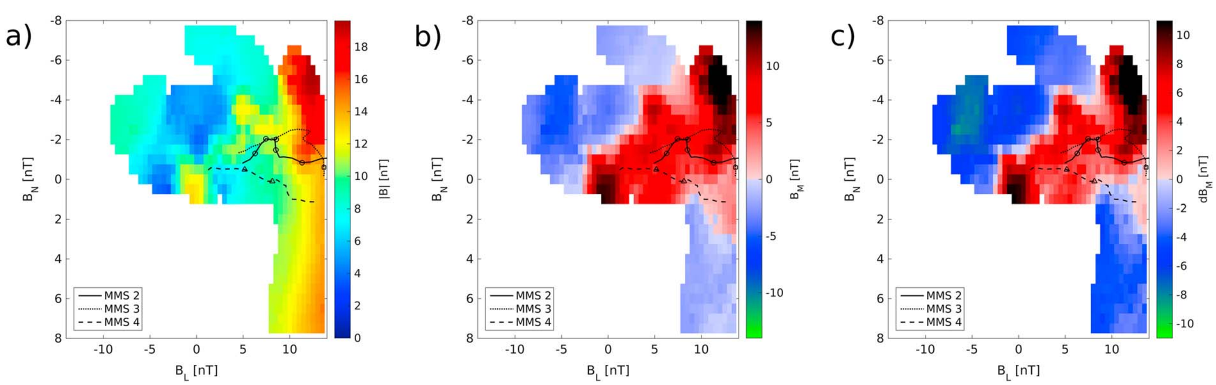

Figure 4. Magnetic field data plotted in parametric space. (a) Magnitude of magnetic field ($|B|$), (b) out-of-plane magnetic field (B_M), and (c) perturbed out-of-plane magnetic field ($\mathrm{d}B_M$) assuming 3.3 nT guide field. The black lines indicate the paths of MMS 2–4 during the time when *Burch et al.* [2016] reported crescent-shaped electron distributions; the marks indicate the location where each crescent was observed.

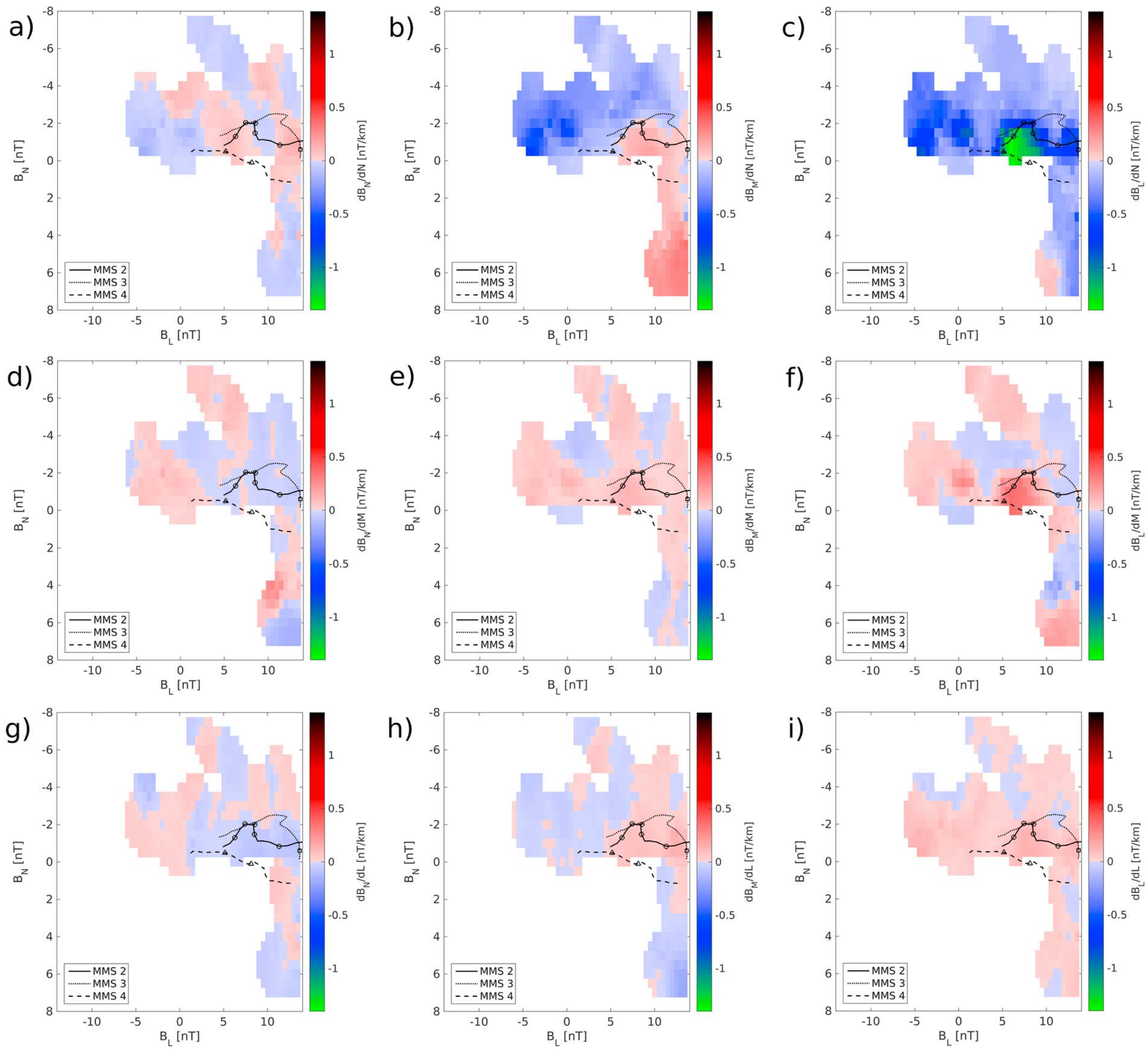

Figure 5. Magnetic fields observed across the MMS tetrahedron. The position in parametric space is based on the tetrahedron mean field. (a) dB_N/dN, (b) dB_M/dN, (c) dB_L/dN, (d) dB_N/dM, (e) dB_M/dM, (f) dB_L/dM, (g) dB_N/dL, (h) dB_M/dL, and (i) dB_L/dL. The black lines indicate the paths of MMS 2–4 during the time when *Burch et al.* [2016] reported crescent-shaped electron distributions; the plot markers indicate the location where each crescent was observed.

appearance but serves to highlight a region of strong, negative, out-of-plane magnetic field located on the magnetosheath side between $-7.5 < B_L < -3.5$ nT and $-5 < B_N < -1.5$ nT.

The gradients in the magnetic field, as seen across the MMS tetrahedron, can be found in Figure 5. Along the N direction, Figures 5a–5c, we can observe significant and consistent gradients in dB_M/dN (b) and dB_L/dN (c). The gradient dB_L/dN, Figure 5c, is negative across the parametric space, and between $5.5 < B_L < 8.5$ nT and $-1.5 < B_N < 0$ nT the gradient exhibits a negative enhancement with a peak value of -1.5 nT/km. The gradients in the M direction, Figures 5d–5f, are weak, and with the exception of dB_L/dM it does not exhibit any consistent trends. Between $5.5 < B_L < 8.5$ nT and $-1.5 < B_N < 0$ nT the gradient is a factor of 2 stronger than in the surrounding areas, with a peak value of approximately 0.4 nT/km. The gradients in the L direction, Figures 5g–5i, do not exhibit any clear features.

Figure 6 illustrates the electric field across the parametric space. As can be seen in Figure 6a, E_N is generally weak, $|E_N| < 2$ mV/m, but exhibits a strong enhancement on the magnetospheric side at $4.5 < B_L < 9.5$ nT and $-2.5 < B_N < 1$ nT. In this region E_N has an average value of approximately 7 mV/m, with a peak value of approximately 15 mV/m at ($B_L = 6.5$ nT, $B_N = -2$ nT). Just outside of this region of strong positive B_N, toward the magnetosheath, we can observe a region of negative E_N of approximately -2 mV/m.

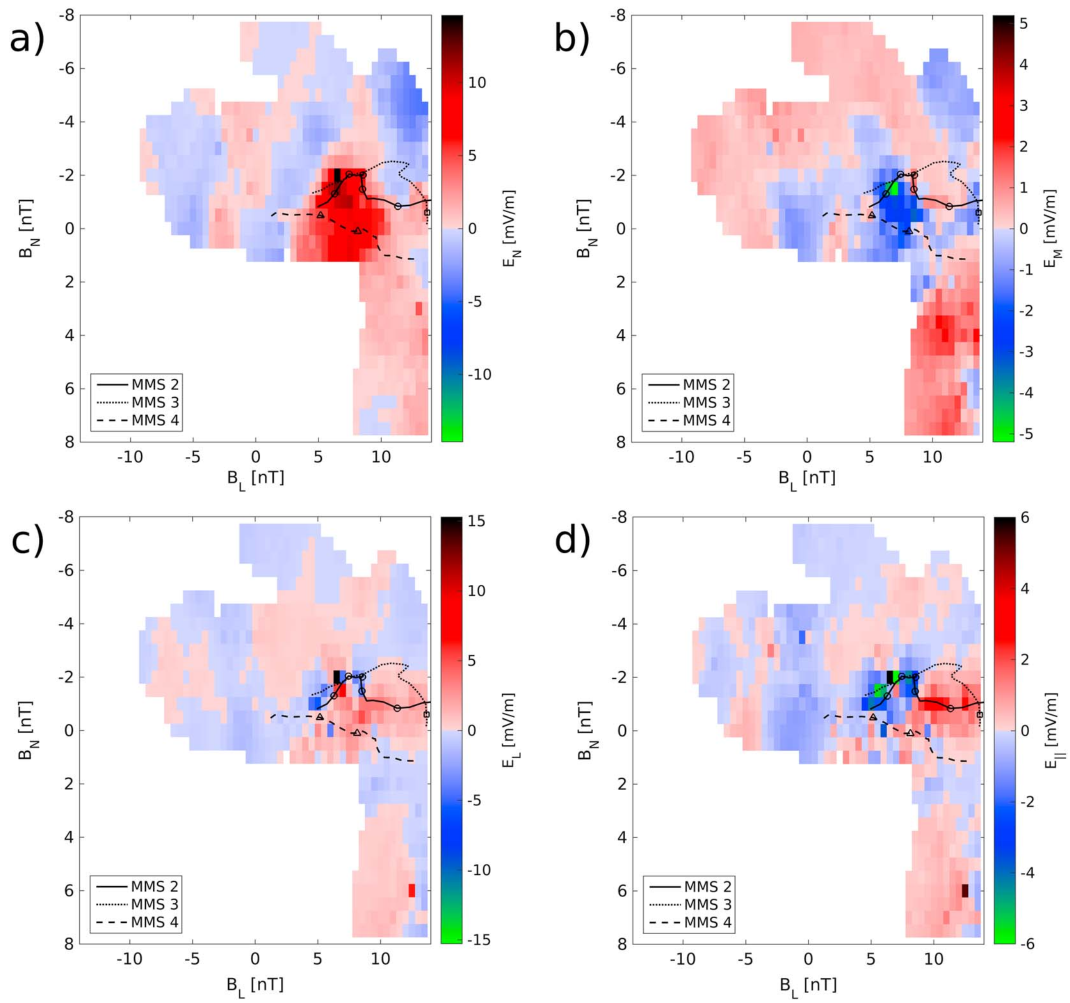

Figure 6. Electric field data plotted in parametric space. (a) Nelectric field (E_N), (b) out-of-plane electric field (E_M), (c) tangential electric field (E_L), and (d) parallel electric field ($E_{||}$). The black lines indicate the paths of MMS 2–4 during the time when *Burch et al.* [2016] reported crescent-shaped electron distributions; the plot markers indicate the location where each crescent was observed.

In general, the out-of-plane electric field, E_M, is positive, $|E_M| < 2$ mV/m, and exhibits only minor variations across the parametric space. The main exception is found on the magnetosphere side, between $5.5 < B_L < 8$ nT and $-2 < B_N < 0.5$ nT. Here the average E_M is approximately −3 mV/m, with a negative peak at ($B_L = 7$ nT, $B_N = -1.5$ nT), where $E_M < -5$ mV/m.

In most of the parametric space $|E_L|$ is a few mV/m, making it the weakest of the electric field components. The area between $4.5 < B_L < 8$ nT and $-2 < B_N < 0$ nT exhibits $|E_L| > 10$ mV/m with a preference for negative electric field on the northern side of this area and vice versa.

The parallel electric field, Figure 6d, exhibits two areas with enhancements. Between $4.5 < B_L < 8.5$ nT and $-2 < B_N < 0.5$ nT, the parallel electric field is negative (anti−field aligned) and from −3 to −6 mV/m. Farther toward the magnetosphere, between $9.5 < B_L < 11$ nT and $-1.5 < B_N < 0$ nT, the parallel electric field is mainly field aligned and 2–4 mV/m. In addition, at two points ($B_L = 6$ nT, $B_N = 12.5$ nT) and ($B_L = 6.5$ nT, $B_N = -2$ nT), the parallel electric field is positive (field aligned) and in excess of 6 mV/m.

As can be seen in Figure 7a, the parallel energy dissipation in the electron frame is generally low, $|\mathbf{j}'_{||} \cdot \mathbf{E}'_{||}| < 0.2$ nW/m^3. At ($B_L = 5.5$ nT, $B_N = 0$ nT), we observe a local maximum where $\mathbf{j}'_{||} \cdot \mathbf{E}'_{||}$ is 2 nW/m^3, surrounded by a small area where $\mathbf{j}'_{||} \cdot \mathbf{E}'_{||} > 0.5$ nW/m^3. We can observe three local minima where $\mathbf{j}'_{||} \cdot \mathbf{E}'_{||} < -0.5$ nW/m^3 located at ($B_L = 1.5$ nT, $B_N = -0.5$ nT), ($B_L = 4$ nT, $B_N = -1$ nT), and ($B_L = 5.5$ nT, $B_N = 0$ nT).

The perpendicular energy dissipation can be seen in Figure 7b. Throughout our parametric space the energy dissipation is typically < 1 nW/m^3. Around $6 < B_L < 10$ nT and $-2 < B_N < -0.5$ nT, we have several instances

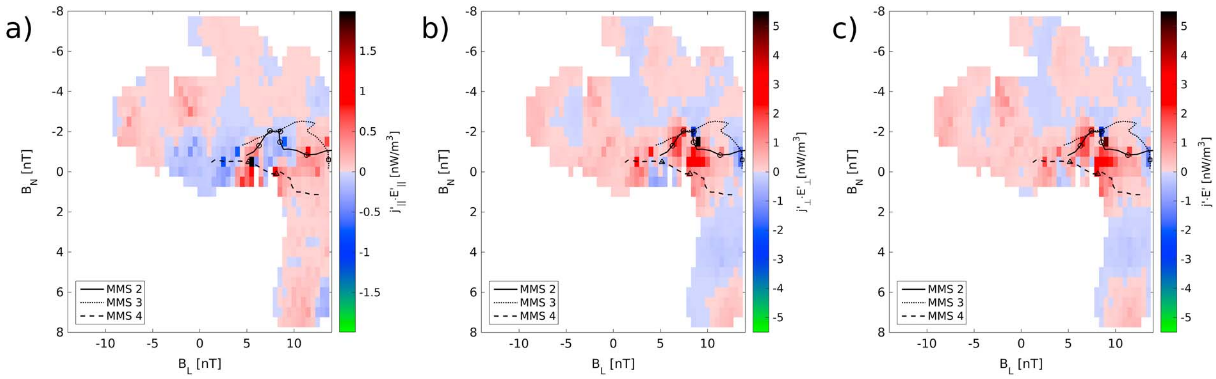

Figure 7. Energy dissipation in the electron rest frame plotted in parametric space. (a) Dissipation parallel to the magnetic field, (b) dissipation perpendicular to the magnetic field, and (c) total energy dissipation. The black lines indicate the paths of MMS 2–4 during the time when *Burch et al.* [2016] reported crescent-shaped electron distributions; the plot markers indicate the location where each crescent was observed.

of $|\mathbf{j}'_\perp \cdot \mathbf{E}'_\perp| > 3$ nW/m^3 with a maximum of 5.5 nW/m^3 at ($B_L = 9$ nT, $B_N = -1.5$ nT). In this region there are several individual measurements of $\mathbf{j}'_\perp \cdot \mathbf{E}'_\perp > 10$ nW/m^3. This area is where *Burch et al.* [2016] report observing electron crescents. In addition, we can observe a pronounced minimum of approximately −2.5 nW/m^3 located at ($B_L = 8.5$ nT, $B_N = -2$ nT).

The distribution of the total energy dissipation closely resembles that of the perpendicular energy dissipation (see Figure 7c). This is a consequence of it being a factor of 2–3 larger than the parallel energy dissipation.

As can be seen in Figure 8a, the temperature anisotropy ($T_{||}/T_\perp$) is typically larger on the magnetospheric side, exhibiting a wedge-like structure with $T_{||}/T_\perp > 1$ pointing toward the X line. Starting at the X line, we can observe another wedge-shaped area extending northward, where $T_{||}/T_\perp \leq 1$.

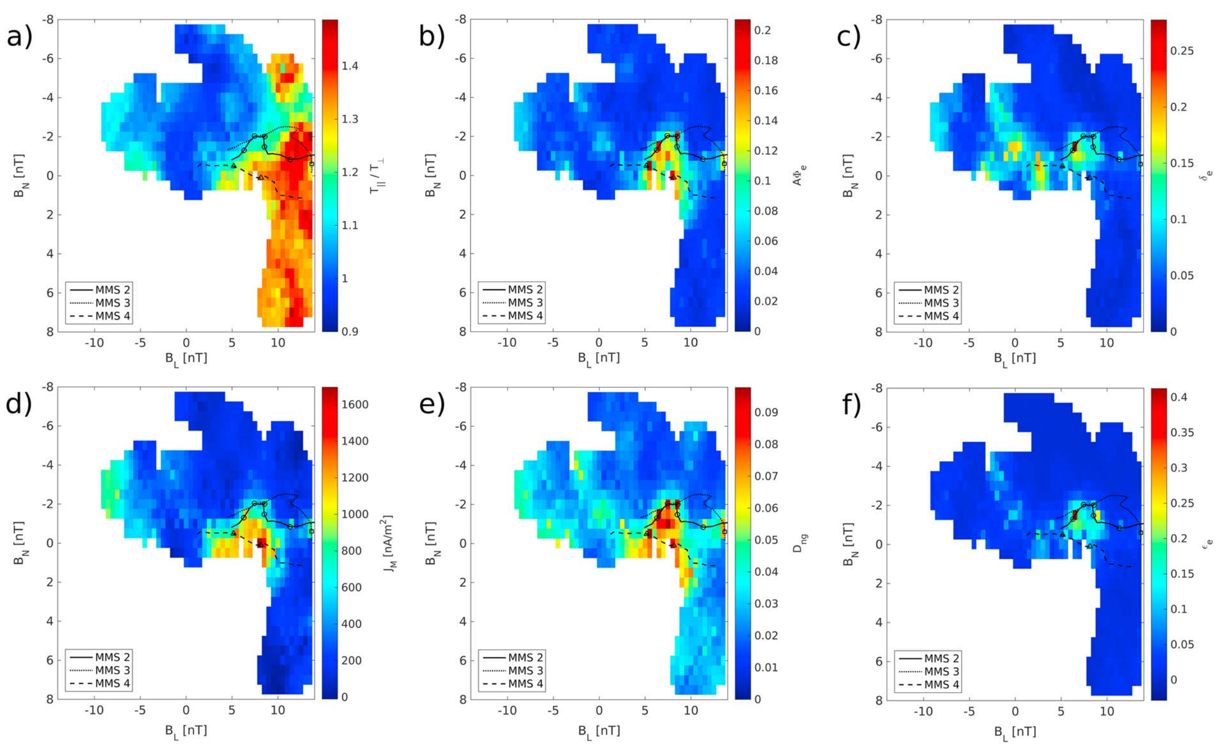

Figure 8. Electron moments data plotted in parametric space. (a) Temperature anisotropy ($T_{||}/T_\perp$), (b) pressure agyrotropy ($A\Phi_e$), (c) ratio of electric and magnetic forces (δ_e), (d) out-of-plane current ($\mathbf{j}_M$), (e) pressure nongyrotropy (D_{ng}), and (f) rate of electron energization (ϵ_e). The black lines indicate the paths of MMS 2–4 during the time when *Burch et al.* [2016] reported crescent-shaped electron distributions; the plot markers indicate the location where each crescent was observed.

Figures 8b and 8e show that both the electron pressure agyrotropy ($A\Phi_e$) and nongyrotropy (D_{ng}) are enhanced in a region between $5 < B_L < 9.5$ nT and $-2 < B_N < 1$ nT. The peak values of $A\Phi_e$ and D_{ng} are 0.18 and 0.1, respectively. Both D_{ng} and $A\Phi_e$ exhibit local maxima in the locations where *Burch et al.* [2016] report observing electron crescents. In addition, $A\Phi_e$, but more prominently so D_{ng}, exhibits a weak enhancement, forming a line starting at ($B_L = 1.5$ nT, $B_N = -0.5$ nT), extending northward and toward the magnetosheath.

The ratio of electric and magnetic forces (δ_e), Figure 8c, exhibits three local maxima with the most pronounced one being located at ($B_L = 8$ nT, $B_N = -1.5$ nT), where $\delta_e > 0.3$. In addition, δ_e exhibits a weak enhancement, forming a line starting at ($B_L = 1.5$ nT, $B_N = -0.5$ nT), extending northward and toward the magnetosheath. Along this line, at ($B_L = -0.8$ nT, $B_N = -1.2$ nT), MMS 2 made a single observation where $\delta_e > 1$, which indicates that the electrons are fully demagnetized [*Maynard et al.*, 2012; *Scudder et al.*, 2012].

As seen in Figure 8f, the rate of electron energization (ϵ_e) exhibits a pattern which somewhat resembles that of δ_e. The maximum rate of energization is in excess of 0.4, which corresponds with an electron increasing its energy by 40% over the course of one cyclotron period. This maximum is located at ($B_L = 8$ nT, $B_N = -1.5$ nT) which coincides with a the peak in δ_e. Similarly, ϵ_e exhibits a series of weak enhancement, along a line starting at ($B_L = 1.5$ nT, $B_N = -0.5$ nT), extending northward and toward the magnetosheath. Though this structure is not as pronounced as it is for δ_e.

The out-of-plane current (j_M), Figure 8d, exhibits an enhancement at $2.5 < B_L < 9.5$ nT and $-1.5 < B_N < 1$ nT. Here the current is approximately 1200 nA/m^2 with a peak value of 1700 nA/m^2 located at ($B_L = 8$ nT, $B_N = 0$ nT).

4. Discussion

As can be seen in Figures 4–8, the MMS satellites are mostly located north of the X line, except when they are well toward the magnetosphere where $B_L > 7$ nT. This complicates the analysis as we cannot fully study many of the symmetries/asymmetries associated with dayside reconnection.

The clover leaf-shaped area with low magnetic field strength, observed in Figure 4a, is similar to what has been observed in 2-D PIC simulations of asymmetric reconnection. Where it was caused by the Hall magnetic field along the magnetosheath separatrix [*Pritchett and Mozer*, 2009a], which is consistent with our observations. However, the enhancement in the magnetic field strength and out-of-plane magnetic field seen near the X line does not appear to be consistent with a Hall magnetic field. It has been suggested that the reconnection plane can be tilted near the X line [*Hesse et al.*, 2008; *Mozer and Pritchett*, 2011]. Since the orientation of reconnection plane at the magnetopause and at the X line plane differs, the conversion of the magnetic field into boundary-normal coordinates would result in an enhanced out-of-plane component.

The linear structure of enhance positive B_M, starting at the X line and extending northward and toward the magnetosphere, occurs where we expect to find the separatrix of our model topology, near the boundary between a predominately tangential and a predominately normal magnetic field, which in the parametric space plots corresponds to diagonal lines going through the origin. It is of approximately the same magnitude as the negative Hall field observed of the magnetosheath side, which is not expected for asymmetric reconnection where the Hall field is typically stronger on the magnetosheath side [*Pritchett and Mozer*, 2009a; *Mozer and Pritchett*, 2011]. This could in part be due to the small but finite guide field enhancing the Hall field. However, the lack of data from south of the X line makes comparisons difficult and prevents drawing any definitive conclusions.

The calculation of the magnetic gradients is done under the assumption of linearity between satellites. One way of estimating the errors introduced by nonlinearity is to calculate the divergence of the magnetic, which ideally is to be zero. Throughout the parametric space the average of $|\nabla \cdot \mathbf{B}|$ is 0.05 nT/km. With the exceptions of $\mathrm{d}B_M/\mathrm{d}L$, $\mathrm{d}B_L/\mathrm{d}N$, and $\mathrm{d}B_L/\mathrm{d}M$, the observed gradients are not strong enough compared to the $\nabla \cdot \mathbf{B}$ to exclude the possibility that they are caused by noise and artifacts due to nonlinearity. This prevents us from recovering the corresponding spatial scale of our parametric space. As a consequence, we cannot perform calculations which require knowledge of the spatial scale, such as tracing magnetic field lines or integrating the electric field to calculate the electric potential. The weak magnetic gradients in along the *M* direction is indicative of a mostly 2-D geometry. However, between $5.5 < B_L < 8.5$ nT, $-1.5 < B_N < 0$ nT we can observe an area of enhanced $\mathrm{d}B_L/\mathrm{d}M$, which could indicate a 3-D geometry. The clear and consistent negative $\mathrm{d}B_L/\mathrm{d}N$

gradient is consistent with the expected transition from negative B_L on the magnetosheath side and positive B_L on the magnetospheric side.

As is seen in Figure 6a, we observe a positive enhancement in E_N with a peak value of approximately 7 mV/m. This enhancement is located on the magnetospheric side of the X line, at $4.5 < B_L < 9.5$ nT and $-2.5 < B_N < 1$ nT, pointing toward the X line. On the magnetosheath side of this enhancement we see a region with negative E_N of 1 to 2 mV/m. The observation of a stronger Hall electric field on the magnetosphere side is consistent with Hall electric fields seen in simulations of asymmetric reconnection [*Mozer et al.*, 2008; *Pritchett and Mozer*, 2009a; *Mozer and Pritchett*, 2011; *Muzamil et al.*, 2014]. In contrast to symmetric reconnection, the Hall electric field in asymmetric does not point toward the X line but rather toward the flow stagnation point, which for asymmetric reconnection is expected to be located on the magnetosphere side of the X line [*Cassak and Shay*, 2007; *Birn et al.*, 2008]. The Hall electric field exhibits the largest magnitude of the electric fields, between 5 and 15 mV/m, which is in agreement with previous observations from Cluster of some tens of mV/m [*Wygant et al.*, 2005; *Eastwood et al.*, 2010; *Muzamil et al.*, 2014]. The presence of a Hall electric field is associated with the ion diffusion region.

The areas exhibiting smooth and positive E_M with a magnitude of < 2 mV/m are consistent with that of the reconnection electric field, convecting magnetic field lines toward the stagnation point. However, the area around $-2 < B_N < 0.5$ nT and $5.5 < B_L < 8$ nT exhibits a negative, patchy, out-of-plane electric field which is not consistent with the typical reconnection electric field. This negative E_M is not caused by a single peak being propagated to adjacent bins due to the averaging process, as it is already present in the data before the moving average is applied. As can be seen in Figure 6d, this region exhibits a parallel electric field. This indicates that the electric field no longer is that of ideal MHD ($\mathbf{E} = \mathbf{v}\times\mathbf{B}$). This indicates that E_M is not simply the classic reconnection electric field. Comparisons with Figure 4 show that the magnetic field has a significant component in the M direction. This is caused by the presence of a guide field as well as the Hall magnetic field. Therefore, the parallel electric field will have a significant component along the M direction. In the region in question the M component of the parallel electric field is approximately -3 mV/m, which is the same as what we have seen in Figure 6b. It is therefore likely that parallel electric field is the cause of the negative E_M.

The negative (anti–field aligned) parallel electric field observed north of the X line, seen in Figure 6d, is consistent with the general picture of the electron diffusion region and the parallel electric field generating the electron jets. However, the region of positive (field aligned) parallel electric fields is offset in the magnetospheric direction rather than southward as one might expect. Since we have few observations from south of the X line, especially in this region, we cannot determine if we are seeing the expected bipolar parallel electric field signature, but with a tilted symmetry axis, or if the two areas enhanced parallel electric field are unrelated.

Figure 7 shows that in the region where we observe the peaks in δ_e and ϵ_e there are two processes responsible for energizing the electrons. There is a conversion of parallel energy into perpendicular energy as well as a large net energy gain caused by the conversion of magnetic energy into electron energy. This behavior has been observed in numerical simulations of asymmetric reconnection [*Pritchett and Mozer*, 2009b].

It is worth noting that while the three local maxima in δ_e exhibit relatively similar values, they have arisen from different physics. By reviewing equation (3) we see that large δ_e is caused by a strong electric field in the electron frame, $\mathbf{E} + \mathbf{v} \times \mathbf{B}$, weak magnetic field, or a combination thereof. The two local maxima near the X line coincide with local minima in the magnetic field strength of approximately 4 nT. In contrast, the global maximum in δ_e located at ($B_L = 8$ nT, $B_N = -1.5$ nT) occurs in a region where the magnetic field strength is approximately 12 nT, a factor of 3 larger, implying that the electric fields in the electron frame are considerably larger here.

The similarities between δ_e and ϵ_e, Figures 8c and 8f, are expected as both describe violations of guiding center theory (GCT). In some cases the two are combined into a single parameter describing the degree of GCT violation, κ_e, which is the maximum of δ_e and ϵ_e [*Scudder et al.*, 2012].

The distribution of temperature anisotropy, Figure 8a, exhibits the expected variations with $T_{||}/T_\perp > 1$ in the two inflows and $T_{||}/T_\perp < 1$ in the outflow region [*Egedal et al.*, 2012; *Chen et al.*, 2008; *Le et al.*, 2010]. The clear boundary between areas where $T_{||}/T_\perp < 1$ and $T_{||}/T_\perp > 1$ indicates that the separatrices are located in the expected region. Simulations have shown that the magnetosheath separatrix is associated with enhancements in $D_{\rm ng}$, $A\Phi_e$, δ_e, and ϵ_e [*Scudder and Daughton*, 2008; *Scudder et al.*, 2008; *Aunai et al.*, 2013]. This is similar to the linear structures, starting at ($B_L = 1.5$ nT, $B_N = -0.5$ nT) extending northward and toward the magnetosheath, which are seen in Figures 8b, 8c, 8e, and 8f. These structures follow the expected separatrix but are located on the magnetospheric side of it. However, this could be due to the errors involved in mapping the data to parametric space.

The satellites' path through the parametric space are similar but not identical to those reported by *Denton et al.* [2016]. Both models find that the satellites start on the magnetospheric side of the X line before doing an outward pass, followed by an inward pass near the X line. However, we observe a greater difference between the four satellites, which is expected. Determining the position of the satellites using the velocity of the X line, as is the case in *Denton et al.* [2016], means that all satellites have identical motion but their position is offset. In contrast, parametric mapping means that both spatial and temporal variations in the magnetic topology influence the satellites' predicted position in parametric space. In other words, if two satellites pass through the exact same point in space, at different times, they can observe different magnetic fields and thus have different positions in parametric space.

5. Conclusions

The energy dissipation, agyrotropy, nongyrotropy, rate of electron energization, ratio of electric and magnetic forces, and out-of-plane current all exhibit their peak values on the magnetosphere side of the X line, in the range of $5 < B_L < 8$ nT.

The out-of-plane current, j_M, peaks at $B_N = 0$ nT and exhibits no obvious north-south asymmetry. In contrast, energy dissipation, agyrotropy, nongyrotropy, rate of electron energization and the ratio of electric, and magnetic forces all exhibit their peak values north of the X line, around $-2 < B_N < 0$ nT.

Based on the combined data material, we draw the conclusion that the electron diffusion region was located in the area $6 < B_L < 8$ nT and $-2 < B_N < 0$ nT. From this it is clear that the EDR does not coincide with the topological X line but is located toward the magnetosphere side. This has been predicted in several simulations of asymmetric reconnection [e.g., *Cassak and Shay*, 2007; *Birn et al.*, 2008]. This coincides with the area where *Burch et al.* [2016] reported observing crescent-shaped electron distributions, which are associated with the EDR. The observed north-south asymmetry is not large enough to draw the conclusion whether this is a real north-south asymmetry or a consequence of the difficulties in determining the normal direction of the reconnection plane [*Mozer and Pritchett*, 2011].

The spatial extent of the EDR can be estimated by comparing its extent in parametric space with the observed gradients in the magnetic field. Near the EDR, the gradient dB_L/dN is between -1 and -1.5 nT/km and the B_L extent of the EDR in parametric space is 2 nT. This corresponds the EDR having an extent in the normal direction of between 2 and 3 km on the order of the electron inertial length, $d_e = 1.5-2$ km.

Similarly, the extent in the L direction can be estimated from the B_N/dL gradient, which is approximately -0.1 nT/km. This corresponds to the EDR extending 20 km north of the X line, on the order of 10 d_e or about twice the spacecraft separation. Seeing that MMS 2 passes through the northern parts of the EDR and MMS 4 through the southern parts, we can estimate the extent to be on the order of the spacecraft separation, approximately 10 km.

The weak gradients along the M direction indicate that much of reconnection region can be adequately described using 2-D models. The enhancement in dB_L/dM near the EDR indicates a 3-D geometry in this small area. This indicates that while a majority of the reconnection region can be simulated in 2-D, the EDR may require 3-D simulations.

Changes in the magnetic topology lie at the heart of magnetic reconnection, and parametric space mapping succeeds in capturing many of the signatures associated with magnetic reconnection and the electron diffusion region. Since the method does not require complicated motion analysis assuming constant or assumptions of constant velocity/acceleration of the satellites, it can achieve a more nuanced description of the satellites' paths.

Since parametric space mapping offers a quantitative estimate of the satellite's position, it reduces the degree of observer bias associated with more qualitative methods. Magnetic field measurement is a readily available product from plasma physics experiments and simulations. This makes it possible to use parametric space mapping for comparing data from different events, different satellites, or with computer simulations.

In summary, this paper serves as a first benchmark of the method showing that has promise of being a useful tool for understanding the physics of magnetic reconnection. However, it still requires further testing and development to be considered a fully matured method.

Acknowledgments
This paper would not have been possible without the data provided by the MMS Team. All data are publicly available at MMS Science Data Center (https://lasp.colorado.edu/mms/sdc/public/). This work was supported by NASA via contract 499878Q.

References

Aunai, N., M. Hesse, and M. Kuznetsova (2013), Electron nongyrotropy in the context of collisionless magnetic reconnection, *Phys. Plasmas*, *20*(9), 092903.

Birn, J., J. Borovsky, and M. Hesse (2008), Properties of asymmetric magnetic reconnection, *Phys. Plasmas*, *15*(3), 032101.

Burch, J., T. Moore, R. Torbert, and B. Giles (2016), Magnetospheric multiscale overview and science objectives, *Space Sci. Rev.*, *199*(1–4), 5–21.

Cassak, P., and M. Shay (2007), Scaling of asymmetric magnetic reconnection: General theory and collisional simulations, *Phys. Plasmas*, *14*(10), 102114.

Chen, L.-J., et al. (2008), Evidence of an extended electron current sheet and its neighboring magnetic island during magnetotail reconnection, *J. Geophys. Res.*, *113*, A12213, doi:10.1029/2008JA013385.

Denton, R. E., B. U. Ö. Sonnerup, H. Hasegawa, T. D. Phan, C. T. Russell, R. J. Strangeway, B. L. Giles, D. Gershman, and R. B. Torbert (2016), Motion of the MMS spacecraft relative to the magnetic reconnection structure observed on 16 october 2015 at 1307 UT, *Geophys. Res. Lett.*, *43*, 5589–5596, doi:10.1002/2016GL069214.

Eastwood, J., M. Shay, T. Phan, and M. Øieroset (2010), Asymmetry of the ion diffusion region hall electric and magnetic fields during guide field reconnection: Observations and comparison with simulations, *Phys. Rev. Lett.*, *104*(20), 205001.

Egedal, J., W. Daughton, and A. Le (2012), Large-scale electron acceleration by parallel electric fields during magnetic reconnection, *Nat. Phys.*, *8*(4), 321–324.

Ergun, R. E., et al. (2016), The axial double probe and fields signal processing for the MMS mission, *Space Sci. Rev.*, *199*(1), 167–188, doi:10.1007/s11214-014-0115-x.

Haaland, S., et al. (2004), Four-spacecraft determination of magnetopause orientation, motion and thickness: Comparison with results from single-spacecraft methods, *Ann. Geophys.*, *22*, 1347–1365.

Hesse, M., M. Kuznetsova, K. Schindler, and J. Birn (2005), Three-dimensional modeling of electron quasiviscous dissipation in guide-field magnetic reconnection, *Phys. Plasmas*, *12*(10), 100704.

Hesse, M., S. Zenitani, and A. Klimas (2008), The structure of the electron outflow jet in collisionless magnetic reconnection, *Phys. Plasmas*, *15*(11), 112102.

Hesse, M., N. Aunai, D. Sibeck, and J. Birn (2014), On the electron diffusion region in planar, asymmetric, systems, *Geophys. Res. Lett.*, *41*, 8673–8680, doi:10.1002/2014GL061586.

Le, A., J. Egedal, W. Daughton, J. Drake, W. Fox, and N. Katz (2010), Magnitude of the hall fields during magnetic reconnection, *Geophys. Res. Lett.*, *37*, L03106, doi:10.1029/2009GL041941.

Le Contel, O., et al. (2016), The search-coil magnetometer for MMS, *Space Sci. Rev.*, *199*(1), 257–282, doi:10.1007/s11214-014-0096-9.

Lindqvist, P.-A., et al. (2016), The spin-plane double probe electric field instrument for MMS, *Space Sci. Rev.*, *199*(1), 137–165, doi:10.1007/s11214-014-0116-9.

Maynard, N. C., C. J. Farrugia, W. J. Burke, D. M. Ober, F. S. Mozer, H. Rème, M. Dunlop, and K. D. Siebert (2012), Cluster observations of the dusk flank magnetopause near the sash: Ion dynamics and flow-through reconnection, *J. Geophys. Res.*, *117*, A10201, doi:10.1029/2012JA017703.

Mozer, F., S. Bale, and T. Phan (2002), Evidence of diffusion regions at a subsolar magnetopause crossing, *Phys. Rev. Lett.*, *89*(1), 015002.

Mozer, F., P. Pritchett, J. Bonnell, D. Sundkvist, and M. Chang (2008), Observations and simulations of asymmetric magnetic field reconnection, *J. Geophys. Res.*, *113*, A00C03, doi:10.1029/2008JA013535.

Mozer, F. S., and P. L. Pritchett (2011), Electron physics of asymmetric magnetic field reconnection, *Space Sci. Rev.*, *158*(1), 119–143.

Muzamil, F., C. Farrugia, R. Torbert, P. Pritchett, F. Mozer, J. Scudder, C. Russell, P. Sandholt, W. Denig, and L. Wilson (2014), Structure of a reconnection layer poleward of the cusp: Extreme density asymmetry and a guide field, *J. Geophys. Res. Space Physics*, *119*, 7343–7362, doi:10.1002/2014JA019879.

Nagai, T., I. Shinohara, M. Fujimoto, M. Hoshino, Y. Saito, S. Machida, and T. Mukai (2001), Geotail observations of the hall current system: Evidence of magnetic reconnection in the magnetotail, *J. Geophys. Res.*, *106*(A11), 25,929–25,949.

Paschmann, G., and P. W. Daly (Eds.) (1998), *Analysis Methods for Multi-Spacecraft Data*, 1.1 ed., ESA Publ. Div., Noordwijk, Netherlands.

Paschmann, G., and P. W. Daly (Eds.) (2008), *Multi-Spacecraft Analysis Methods Revisited*, ESA Publ. Div., Noordwijk, Netherlands.

Pollock, C., et al. (2016), Fast plasma investigation for magnetospheric multiscale, *Space Sci. Rev.*, *199*(1), 331–406, doi:10.1007/s11214-016-0245-4.

Pritchett, P. (2008), Collisionless magnetic reconnection in an asymmetric current sheet, *J. Geophys. Res.*, *113*, A06210, doi:10.1029/2007JA012930.

Pritchett, P. L., and F. S. Mozer (2009a), Asymmetric magnetic reconnection in the presence of a guide field, *J. Geophys. Res.*, *114*, A11210, doi:10.1029/2009JA014343.

Pritchett, P. L., and F. S. Mozer (2009b), The magnetic field reconnection site and dissipation region, *Phys. Plasmas*, *16*(8), 080702, doi:10.1063/1.3206947.

Russell, C. T., et al. (2016), The magnetospheric multiscale magnetometers, *Space Sci. Rev.*, *199*(1), 189–256, doi:10.1007/s11214-014-0057-3.

Scudder, J., and W. Daughton (2008), "Illuminating" electron diffusion regions of collisionless magnetic reconnection using electron agyrotropy, *J. Geophys. Res.*, *113*, A06222, doi:10.1029/2008JA013035.

Scudder, J., R. Holdaway, R. Glassberg, and S. Rodriguez (2008), Electron diffusion region and thermal demagnetization, *J. Geophys. Res.*, *113*, A10208, doi:10.1029/2008JA013361.

Scudder, J., R. Holdaway, W. Daughton, H. Karimabadi, V. Roytershteyn, C. Russell, and J. Lopez (2012), First resolved observations of the demagnetized electron-diffusion region of an astrophysical magnetic-reconnection site, *Phys. Rev. Lett.*, *108*(22), 225005.

Sonnerup, B. U. O. (1979), Magnetic field reconnection, *Solar Syst. Plasma Phys.*, *1*, 45–108.

Torbert, R. B., et al. (2016a), The fields instrument suite on MMS: Scientific objectives, measurements, and data products, *Space Sci. Rev.*, *199*(1–4), 105–135.

Torbert, R. B., et al. (2016b), Estimates of terms in Ohm's law during an encounter with an electron diffusion region, *Geophys. Res. Lett.*, *43*, 5918–5925, doi:10.1002/2016GL069553.

Torbert, R. B., et al. (2016c), The electron drift instrument for MMS, *Space Sci. Rev.*, *199*(1), 283–305, doi:10.1007/s11214-015-0182-7.

Vaivads, A., Y. Khotyaintsev, M. André, A. Retino, S. Buchert, B. Rogers, P. Décréau, G. Paschmann, and T. Phan (2004), Structure of the magnetic reconnection diffusion region from four-spacecraft observations, *Phys. Rev. Lett.*, *93*(10), 105001.

Vaivads, A., A. Retinò, and M. André (2006), Microphysics of magnetic reconnection, *Space Sci. Rev.*, *122*(1–4), 19–27.

Wygant, J., et al. (2005), Cluster observations of an intense normal component of the electric field at a thin reconnecting current sheet in the tail and its role in the shock-like acceleration of the ion fluid into the separatrix region, *J. Geophys. Res.*, *110*, A09206, doi:10.1029/2004JA010708.

Zenitani, S., M. Hesse, A. Klimas, and M. Kuznetsova (2011a), New measure of the dissipation region in collisionless magnetic reconnection, *Phys. Rev. Lett.*, *106*(19), 195003.

Zenitani, S., M. Hesse, A. Klimas, C. Black, and M. Kuznetsova (2011b), The inner structure of collisionless magnetic reconnection: The electron-frame dissipation measure and hall fields, *Phys. Plasmas*, *18*(12), 122108.